Adiabatic entanglement transport in Rydberg aggregates

Adiabatic entanglement transport in Rydberg aggregates

S Möbius, S Wüster, C Ates, A Eisfeld and J M Rost

Max Planck Institute for the Physics of Complex Systems, Nöthnitzer Strasse 38, 01187 Dresden, Germany

E-mail: sew654@pks.mpg.de

Abstract
We consider the interplay between excitonic and atomic motion in a regular, flexible chain of Rydberg atoms, extending our recent results on entanglement transport in Rydberg chains (Wüster *et al* 2010 *Phys. Rev. Lett.* **105** 053004). In such a Rydberg chain, similar to molecular aggregates, an electronic excitation is delocalized due to long-range dipole–dipole interactions among the atoms. The transport of an exciton that is initially trapped by a chain dislocation is strongly coupled to nuclear dynamics, forming a localized pulse of combined excitation and displacement. This pulse transfers entanglement between dislocated atoms adiabatically along the chain. Details about the interaction and the preparation of the initial state are discussed. We also present evidence that the quantum dynamics of this complex many-body problem can be accurately described by selected quantum–classical methods, which greatly simplify investigations of excitation transport in flexible chains.

(Some figures in this article are in colour only in the electronic version)

1. Introduction

Rydberg atoms have recently received increasing attention in cold atomic physics, to a large part due to their strong long-range interactions, with diverse consequences from dipole blockade [1–3] to long-range molecules [4–6]. Among the interactions in cold Rydberg gases, resonant dipole–dipole interactions [7–9] and their non-resonant variants (van der Waals interactions) [10, 11] are particularly prominent. These interactions enable Rydberg ensembles to simulate the quantum dynamics of other long-range interacting systems, from condensed matter physics [12, 13] to molecular aggregates [9, 14, 15]. We focus on the latter possibility, and explore basic consequences of joint dynamics of atomic motion and excitonic transport.

Within an essential state picture, where only two Rydberg states per atom are taken into account, the transfer of excitation can be adequately described by using the exciton theory of Frenkel [16, 17]. Following the pioneering paper by Franck and Teller [18], this theory has found wide application in describing excitation transfer, e.g. in molecular crystals [19], photosynthesis [20] or organic dye aggregates [21]. In all these systems the coupling between the exciton and nuclear degrees of freedom strongly influences the excitation transfer [18, 22–28]. Similar effects will be reported in this study.

The strong interactions between the monomers of molecular aggregates lead to coherently delocalized entangled states [29–31] which are e.g. responsible for the J-band of organic dye aggregates. Recent experiments indicate robust excitonic coherence even in biological systems, such as photosynthetic complexes [32–34].

In all these excitonic systems the *resonant* nature of the interaction plays a crucial role. Besides the transfer of excitation, this interaction also creates a potential, which for an atom pair depends like $1/R^3$ on their distance R. For Rydberg atoms it has been recognized that this potential can lead to large forces on the individual atoms [15, 35] and thus cause their motion. In contrast to the atomic motion induced by the van der Waals interaction, which is due to strongly off-resonant coupling, the character of the motion (repulsive, attractive or even mixed) in the resonant case depends strongly on the excitonic eigenstates [15]. These in turn depend on the atomic positions, which is why excitation transport and motion become interlinked. In this respect, our setup [15, 36] strongly differs from that in [37], where the effect of *externally enforced* atomic motion on exciton transport is studied.

In this paper, we extend our previous studies of excitons and their dynamics in Rydberg chains [15, 36]. To study exciton dynamics with Rydberg ensembles, one requires strong selectivity of the accessible electronic states of each atom and control over the initial exciton state. We consider both requirements, and furthermore provide additional details on the Newton's cradle-type entanglement transport scenario reported in [36]. Specifically, we vary atomic masses and interaction potentials. For the entanglement transport scenario, we show that two mixed quantum–classical methods are well suited to describe this complex many-body problem: Tully's surface hopping method, and the Ehrenfest method. For short chains, we validate these quantum–classical propagation methods by comparison with a full quantum-mechanical calculation, finding perfect agreement.

The paper is organized as follows. In section 2, we describe which conditions we imply in order to label a Rydberg chain as Rydberg *aggregate*. After a brief comparison with molecular aggregates (section 2.1), we describe our geometric setup and Hamiltonian (section 2.2), illustrate how a simple treatment of transition dipole–dipole interactions can emerge (section 2.3), argue the validity of our essential state model (section 2.4), lay the basis for a description of the Rydberg chain's excitations in terms of excitons and their localization (section 2.5) and show how the initial states for our later applications could be obtained (section 2.6). The final part of section 2 (section 2.7) details the quantum and quantum–classical formalisms used to simultaneously model the dynamics of atomic motion and excitons. After these preparations, we proceed in section 3 to a detailed presentation of the entanglement transport scenario first reported in [36] and survey the parameter space for this scenario in section 4. Some appendices supply further details.

2. Rydberg aggregates

2.1. Brief comparison with molecular aggregates

Since molecular aggregates have been extensively studied over the last 70 years, it is appropriate to briefly juxtapose the Rydberg aggregates with these 'conventional' molecular aggregates.

Molecular aggregates appear in various contexts, ranging from organic crystals [19, 38] over self-assembled cylindrical dye aggregates [39] to complex biological light harvesting systems [20]. These systems range from only two monomers up to thousands of monomers, which can aggregate into various geometrical arrangements. The (resonant) transition dipole–dipole interaction between the monomers leads to entangled states, often accompanied by a drastic change in the absorption spectrum compared to that of the single monomer [21, 29]. Besides some fundamental interest (e.g. in photosynthesis) the extraordinary properties of these aggregates have led to various applications, ranging from sensitizers in photography [40, 41], to the measurement of membrane potentials [42, 43], and cancer therapy [44]. Also in the development of efficient, low-cost artificial light harvesting units (like organic solar cells), dye aggregates might play an important role [45, 46].

In molecular aggregates the monomers are held at their positions and orientations, e.g. by a protein environment or by van der Waals interactions, with distances of the order of a few Ångström. In the Rydberg aggregates investigated here, the distances are of the order of a few micrometers and, most importantly, the Rydberg atoms are free to move. The main difference, however, between molecular aggregates and Rydberg aggregates is the internal structure and the environment. While the Rydberg atoms are at ultra-cold temperatures and interact only weakly with the environment, the electronic excitation in the molecular case does strongly couple to the environment (often at ambient temperature) and a plethora of internal vibrational modes [47]. This typically necessitates various approximations and assumptions in the theoretical description of molecular aggregates, since often details about the environment or even the precise arrangement of the monomers are unknown. Furthermore, due to the small distances, the direct experimental observation of coherent energy transfer in molecular aggregates is challenging. Hence, related investigations are typically of spectroscopic nature [48], and infer the exciton dynamics only indirectly.

In contrast, the beauty of Rydberg aggregates is that individual excitation and manipulation of the atoms can be done more easily. Also, since environment and vibrations do not play a role, it is possible to develop a detailed theoretical description where common approximations can be checked.

2.2. General setup

We study a chain of N identical atoms with mass M and denote the position of the nth atom by $\mathbf{R}_n$. These positions are grouped into a $3N$-dimensional vector $\mathbf{R} = (\mathbf{R}_1, \ldots, \mathbf{R}_N)^T$.[1] In the following we will refer to these coordinates as nuclear coordinates. Each atom should be initially well localized, for example in the ground state of an optical lattice or a micro-lens array [49]. We can then ensure that the distance $R_{nm} \equiv |\mathbf{R}_n - \mathbf{R}_m|$ between the atoms is large enough to neglect the overlap between the electronic wavefunctions of atoms n and m.

Consider a situation where all but one of the N atoms are in a Rydberg state $|\nu s\rangle$, with principal quantum number ν and angular momentum $l = 0$. The remaining atom is in an angular momentum $l = 1$ state $|\nu p\rangle$, which we will call the 'excited' state. We now define the single-excitation Hilbert space, whose electronic part is spanned by

$$|\pi_n\rangle \equiv |s \cdots p \cdots s\rangle, \tag{1}$$

a state in which the atom n is in the p state and all others are in the s state. In figure 1, the state $|\pi_1\rangle$ is sketched for the case $N = 5$. Note that the roles of s and p are more or less interchangeable.

For a clear cut picture of exciton transport, the states (1) should form the essential part of the electronic basis for the whole aggregate. This requires that transitions to other states, such as $|s \cdots p \cdots s \cdots p \cdots s\rangle$ or $|s \cdots d \cdots s\rangle$, are negligible,

---

[1] We present our introductory theory as far as possible in three dimensions (3D). For all our results we only consider one-dimensional motion (1D), assuming that transverse motion is frozen out by the confinement of the atoms.
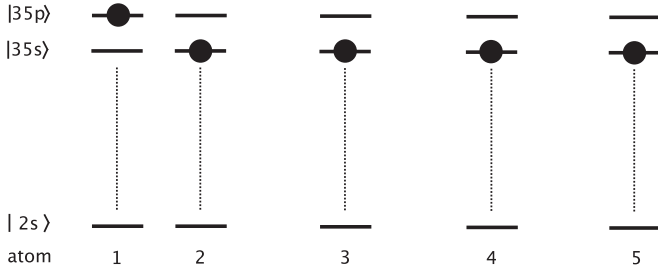
Figure 1. Visualization of the electronic state $|\pi_1\rangle$.

because they are energetically far detuned with respect to the relevant couplings. Then, the only relevant interactions occur within the space spanned by (1) and conserve the number of excitations. In section 2.4 we show by an example that these requirements can be fulfilled.

In terms of the basis (1), our total Hamiltonian describing atomic motion and interactions within the essential states manifold is given in atomic units by

$$H(\mathbf{R}) = -\sum_{n=1}^{N} \frac{\nabla_{\mathbf{R}_n}^2}{2M} + H^{\text{el}}(\mathbf{R}). \tag{2}$$

Here, the electronic Hamiltonian, which depends on the nuclear coordinates, is

$$H^{\text{el}}(\mathbf{R}) = \sum_{nm} V_{nm}(R_{nm})|\pi_n\rangle\langle\pi_m|, \tag{3}$$

where

$$V_{nm}(R_{nm}) = (-1)^{\eta} \frac{\mu^2}{R_{nm}^3} \tag{4}$$

is the dipole–dipole coupling between atoms n and m and R_{nm} their separation. We parameterized the strength of the coupling by its magnitude μ^2 and sign $\eta \in \{0, 1\}$. Due to this resonant dipole–dipole interaction the 'excitation' can be transferred from atom n to m. We outline in section 2.3 why we can avoid a more complicated, angular-dependent [9] expression.

For most specific examples throughout this paper, we consider the atomic species ^{7}Li. Among the work horses of cold atom physics, this atom is one of the lightest and hence most suited to display phenomena of dipole–dipole interaction-induced motion, within the time scales available. Its atomic mass is roughly $M = 11\,000$ au and transition dipole moment has the strength $\mu = 1000$ au between s and p states with a principal quantum number $\nu \approx 30, \ldots, 40$.

In section 4, we survey the response of dynamics dictated by (2) to changes of Hamiltonian parameters. To this end we also generalize the type of interaction, considering $V_{nm}(R_{nm}) = (-1)^{\eta}\mu^2/R_{nm}^{\alpha}$, where α can for example vary from $\alpha = 1, \ldots, 6$, with character of the interaction potentials ranging from Coulombic to van der Waals. Keep in mind though that unlike conventional Coulomb or van der Waals interactions, those considered here would still have a resonant transition character.

2.3. Dipole–dipole interactions

In this section, we outline how the simple form $V_{nm}(R_{nm}) = (-1)^{\eta}\mu^2/R_{nm}^3$ can be obtained for dipole–dipole interactions. For this purpose, we consider a binary atom system with separation $\mathbf{R}_{nm} = \mathbf{R}_m - \mathbf{R}_n$ and define $R = |\mathbf{R}_{nm}|$ and $\hat{\mathbf{R}} = \mathbf{R}_{nm}/R$. We assume that one of the atoms is in a $|\nu s\rangle$ state and the other in a $|\nu p\rangle$ state, where ν is the (large) principal quantum number, subsequently suppressed. As long as one ignores directional effects, the essential state Hilbert space for such two atoms is spanned by $|sp\rangle$, $|ps\rangle$. Considering angular-dependent *transition* dipole–dipole interactions amounts to taking into account also the magnetic quantum number. We then have six essential states: $|\{p, 1\}s\rangle$, $|\{p, 0\}s\rangle$, $|\{p, -1\}s\rangle$, $|s\{p, 1\}\rangle$, $|s\{p, 0\}\rangle$, $|s\{p, -1\}\rangle$, using an obvious notation that writes the magnetic quantum number m of the atom with $l = 1$ within the curly brackets.

The non-vanishing dipole–dipole transition amplitudes between those states are [9]

$$V_{1m,00;00,1m'} = -\sqrt{\frac{8\pi}{3}} \frac{(d_{\nu 1, \nu 0})^2}{R^3} (-1)^{m'}$$
$$\times \begin{pmatrix} 1 & 1 & 2 \\ m & -m' & m'-m \end{pmatrix} Y_{2,m'-m}(\hat{\mathbf{R}}), \tag{5}$$

where $Y_{l,m}$ are spherical harmonics and $(\cdots)$ denotes the Wigner $3j$ coefficient. The matrix element $V_{l_1 m_1, l_2 m_2; l_1' m_1', l_2' m_2'}$ describes a transition between the two-atom states indicated with primed and non-primed subscripts. $d_{\nu 1, \nu 0}$ is the radial overlap-matrix element between the $l = 0$ and $l = 1$ states. We refer to [9] for further details. In matrix form, using the above basis ordering, one obtains

$$V = \begin{bmatrix} 0 & V_{\text{ps}} \\ V_{\text{ps}}^{\dagger} & 0 \end{bmatrix} \tag{6}$$

with sub-matrices

$$V_{\text{ps}} = \frac{\tilde{\mu}^2}{R^3} \begin{bmatrix} \dfrac{3\cos^2\theta - 1}{6} & \dfrac{e^{-i\phi}}{\sqrt{2}}\cos\theta\sin\theta & \dfrac{e^{-2i\phi}\sin^2\theta}{2} \\ \dfrac{e^{i\phi}}{\sqrt{2}}\cos\theta\sin\theta & \dfrac{1 - 3\cos^2\theta}{3} & -\dfrac{e^{-i\phi}}{\sqrt{2}}\cos\theta\sin\theta \\ \dfrac{e^{2i\phi}\sin^2\theta}{2} & -\dfrac{e^{i\phi}}{\sqrt{2}}\cos\theta\sin\theta & \dfrac{3\cos^2\theta - 1}{6} \end{bmatrix}. \tag{7}$$

In this matrix, the element $(V_{\text{ps}})_{ij}$ contains the amplitude of transitions from a state $|\{p, m_j\}s\rangle$ to $|s\{p, m_i\})\rangle$, where $m_i, m_j \in \{1, 0, -1\}$. We used the short-hand $\tilde{\mu}^2 = (d_{n_a 1, n_b 0})^2$. The angles θ and ϕ describe $\hat{\mathbf{R}}$ in a spherical polar coordinate system whose z-axis ($\hat{z}$) is the quantization axis with respect to which the magnetic quantum numbers m is defined. A useful choice of $\hat{z}$ will be given by the polarization direction of the light field used for the initial-state creation, see section 2.6.

We will consider two specific simple cases, assuming a linear Rydberg chain.

Case i. Choose $\hat{z}$ along the direction of the chain. Then, for all distance vectors $\mathbf{R}_{nm}$ we have $\theta = 0$ and

$$V_{\text{ps}} = \frac{\tilde{\mu}^2}{3R^3} \begin{bmatrix} 1 & 0 & 0 \\ 0 & -2 & 0 \\ 0 & 0 & 1 \end{bmatrix}. \tag{8}$$

Thus, the magnetic quantum number of the excitation is conserved. Depending on the selected magnetic quantum number m, we can realize different signs η and magnitudes of the interaction.

Case ii. Choose $\hat{z}$ perpendicular to the direction of the chain, which we assume to be in the $\hat{x}$ direction. We then have (setting $\theta = \pi/2$ and $\phi = 0$)

$$V_{\mathrm{ps}} = \frac{\tilde{\mu}^2}{6R^3} \begin{bmatrix} -1 & 0 & 3 \\ 0 & 2 & 0 \\ 3 & 0 & -1 \end{bmatrix}. \qquad (9)$$

It can be seen that the $m = 0$ state decouples and yields a dipole–dipole interaction transport without angular dependence. For all choices of quantization axis and magnetic quantum state, we finally define the parameter μ^2 used in section 2.2 as the modulus of the factor multiplying R^{-3}. How a specific magnetic quantum number for the excitation can be realized is described in section 2.6.

2.4. Validity of the essential state model

Dipole–dipole transitions in principle do not only take place within the $|\mathrm{sp}\rangle$, $|\mathrm{ps}\rangle$ manifold, but also to other states not included in our essential state picture [9]. Nonetheless, parameters where these other states can be ignored can easily be found, as we demonstrate now.

We exploit that transition probabilities from the two original states to all other di-atomic states are negligibly small due to their energy mismatch or selection rules. In other words, all two-atom states to which a direct dipole–dipole transition is possible are much farther detuned than the strength of the transition matrix element. We will illustrate this argument in the following for $^7\mathrm{Li}$.

Consider the two-atom states $|35, \mathrm{s}\rangle \otimes |35, \mathrm{p}\rangle$, $|35, \mathrm{p}\rangle \otimes |35, \mathrm{s}\rangle$. The two-atom states energetically nearest and connected via a single dipole–dipole transition are $|36, \mathrm{s}\rangle \otimes |34, \mathrm{p}\rangle$, $|34, \mathrm{p}\rangle \otimes |36, \mathrm{s}\rangle$, detuned from our essential states by $\Delta = 8.78$ GHz and connected with a coupling strength of about $V = 65$ MHz.[2] A simple analytical four-state model for detuned Rabi oscillations then predicts population transfer out of the essential-state system of the order of $(V/\Delta)^2 = 5 \times 10^{-5}$ for time scales considered in this paper.

As more rigorous justification of the essential state mode, also accounting for successive, cascaded transitions, we propagated the state $|35, \mathrm{s}\rangle \otimes |35, \mathrm{p}\rangle + |35, \mathrm{p}\rangle \otimes |35, \mathrm{s}\rangle$ (an exciton eigenstate, see section 2.5) with a Hamiltonian that contains all ν, l, m states from $\nu = 34$ to 36, setting all dipole-allowed transition matrix elements V to $V = \mu^2/d^3$ for $\mu = 1000$ au and $d = 2\,\mu$m. This value for μ overestimates almost all transition dipoles and the value for d is the smallest separation occurring in the atomic dynamics of section 3. Within this 'worst-case' scenario, total transitions out of our target essential states manifold are of the order of 1×10^{-4} within 20 μs, which is longer than the simulated time span in section 3.

---

[2] We obtain the lithium state energies using quantum-defect theory as described in [50] and transition strength as outlined in [9] with numerical Numerov calculation of radial overlaps.

Finally, kinetic and potential energies of the dynamics presented in our paper amount to only about 5% of the energetic separation between $|35\mathrm{p}\rangle$ and $|35\mathrm{d}\rangle$.

These estimates, while exemplary, show that there is no general problem with finding physically realistic scenarios with Rydberg atoms that can be described well with our model.

2.5. Excitons, exciton localization and a full aggregate initial state

To gain some insight into the structure of the dynamics induced by the Hamiltonian (2), consider eigenstates of the electronic Hamiltonian

$$H^{\mathrm{el}}(\mathbf{R})|\varphi_k(\mathbf{R})\rangle = U_k(\mathbf{R})|\varphi_k(\mathbf{R})\rangle. \qquad (10)$$

For each $\mathbf{R}$ there are N eigenstates labelled by the index k. Each of these eigenstates can be expanded in terms of the previously introduced basis $|\pi_n\rangle$ as

$$|\varphi_k(\mathbf{R})\rangle = \sum_m c_{km}(\mathbf{R})|\pi_m\rangle. \qquad (11)$$

These eigenstates are termed Frenkel 'excitons' [16, 17] and form an adiabatic (Born–Oppenheimer) basis in the language of molecular physics. The corresponding eigenenergies $U_k(\mathbf{R})$, which also depend parametrically on the nuclear coordinates $\mathbf{R}$, define the adiabatic potential surfaces. As evident from (11), an exciton is a coherent superposition of different localized excitation states.

Now, consider a regular chain of Rydberg atoms with spacing x_0, which is perturbed by a dislocation of two atoms in close mutual proximity (distance a), see figure 3. The interaction between these atoms is much larger than interactions involving the remaining atoms. As a consequence two of the exciton states localize on the dislocation atoms. For $a \ll x_0$, the state whose Born–Oppenheimer surface has a repulsive character [15] can be approximately written as $|\varphi_{\mathrm{rep}}\rangle \approx (|\pi_1\rangle + (-1)^\eta|\pi_2\rangle)/\sqrt{2}$. Such repulsive dimer states are observed e.g. in [8]. In figure 2, the excitonic population on the various atoms as a function of a/x_0 is shown for the case $N = 6$ and different interaction exponents α. Our survey of dynamics presented later requires sufficiently good coherent exciton localization on the dislocation atoms, which lead to our choices of a/x_0 indicated by the vertical black lines in the figure.

We now are in position to discuss the whole initial state of our Rydberg aggregate, describing the electronic state and the position of the atoms. The initial *spatial* wavefunction of each atom is assumed Gaussian with standard deviation σ_0. This resembles an experimental situation where the ground-state atoms are trapped in harmonic potentials prior to their excitation to the Rydberg level, as discussed in the next section. For a sketch of this arrangement, see figure 3.

We take the complete initial wavefunction (i.e. containing nuclear and excitonic degrees of freedom) as

$$|\Psi(t = 0)\rangle = |\varphi_{\mathrm{rep}}(\mathbf{R})\rangle \prod_{n=1}^{N} \phi_{\mathrm{G}}(\mathbf{R}_n), \qquad (12)$$
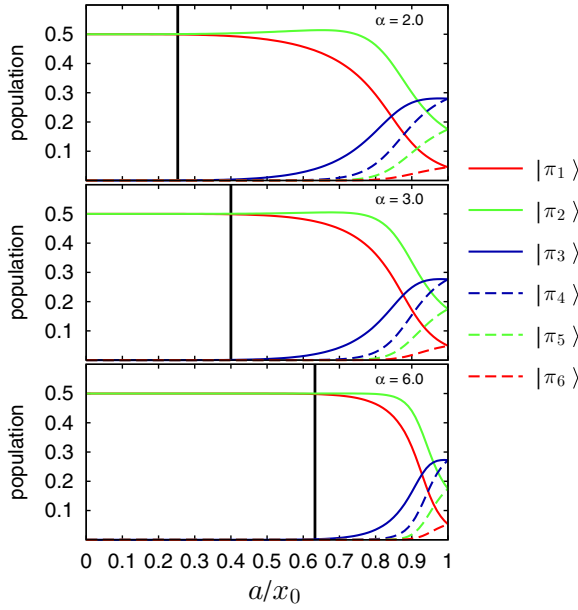
Figure 2. Initial population of the (out of phase) repulsive excitonic state for different α as a function of the dislocation ratio a/x_0. The vertical black line indicates our choices for a/x_0 employed in section 4. Other lines indicate the population in the different excitonic states for a chain containing six Rydberg atoms.
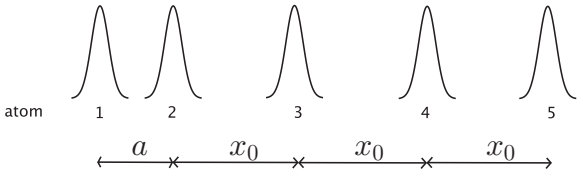

Figure 3. Sketch of the initial total density distribution of Rydberg atoms for the case of $N = 5$ atoms.

$$\phi_G(\mathbf{R}_n) = \mathcal{N} \exp\left(-|\mathbf{R}_n - \mathbf{R}_{0n}|^2/2\sigma_0^2\right), \quad (13)$$

where R_{0n} is the centre of mass of the nth Gaussian and $\mathcal{N}$ is a normalization factor. As above, the index 'rep' denotes the unique exciton state with globally repulsive behaviour [15]. In (12), the exciton state varies with the nuclear coordinates $\mathbf{R}$ within the initial Gaussian distribution, but as long as $\sigma_0 \ll a$ this effect will be small. We found that one obtains almost identical dynamics to that presented in the following, if $\varphi_{\text{rep}}(\mathbf{R})$ is replaced by $\varphi_{\text{rep}}(\mathbf{R_0})$ in (12).

2.6. State preparation

In this section, we will briefly describe how states discussed in the previous section could be prepared experimentally.

At the very beginning, ground state atoms are confined e.g. in optical traps created by microlens arrays that provide the desired spatial arrangement, in our case a linear chain with distances a and x_0. Ideally, there would be exactly one atom per trap site. These ground state atoms are then transferred into a certain Rydberg state (say 35s) via laser excitation[3].

---

[3] If there is more than one atom in the ground state trap, one can ensure, due to dipole blockade, that there is actually only one Rydberg excitation per site.

We now have a state, which we denote by $|s \cdots s\rangle$, where all atoms are in the same Rydberg state $|35s\rangle$. Due to the ultra-cold temperatures the Rydberg atoms can be regarded as frozen during excitation (the distances between the sites have to be chosen such that acceleration and blockade effects due to the van der Waals interaction [51] are negligible). Then, by applying a short microwave pulse, which will be specified below, the eigenstate of the chain $|\psi_{\text{ini}}\rangle \approx (|\pi_1\rangle + |\pi_2\rangle)/\sqrt{2}$ can be excited. To reach $|\psi_{\text{ini}}\rangle \approx (|\pi_1\rangle - |\pi_2\rangle)/\sqrt{2}$ we require a further phase flip described below.

For definiteness we choose the propagation direction of the microwave pulse perpendicular to the chain. Within the dipole approximation the interaction of the atom n with the microwave pulse is given by

$$W_n(t) = -\boldsymbol{\mu}_n \boldsymbol{\mathcal{E}}(t) \quad (14)$$

with the dipole operator $\boldsymbol{\mu}_n$ and electric field $\boldsymbol{\mathcal{E}}(t)$.

Since our target initial electronic state is essentially located on two atoms, in the following we discuss the microwave excitation exemplarily for a dimer. The extension to larger systems can be easily done. In this section, we enlarge our essential state space beyond $|\pi_1\rangle$ and $|\pi_2\rangle$ to also include the 'ground state' $|ss\rangle$ and the doubly excited state $|\{p, m_1\}\{p, m_2\}\rangle$. In this basis the Hamiltonian of the system can be written as

$$H = \begin{bmatrix} 2E_s & \mathbf{W}_1(t) & \mathbf{W}_2(t) & 0 \\ \mathbf{W}_1^\dagger(t) & (E_s + E_p)\mathbf{1}_3 & V_{ps} & \underline{W}_2(t) \\ \mathbf{W}_2^\dagger(t) & V_{ps} & (E_s + E_p)\mathbf{1}_3 & \underline{W}_1(t) \\ 0 & \underline{W}_2^\dagger(t) & \underline{W}_1^\dagger(t) & 2E_p\mathbf{1}_9 \end{bmatrix} \quad (15)$$

with V_{ps} given by (7) and E_s and E_p denoting the energies of the respective Rydberg states. Further, $\mathbf{1}_n$ denotes a $n \times n$ unit matrix, $\mathbf{W}_j(t)$ a 3×1 vector and $\underline{W}_j(t)$ a 3×9 matrix. The components m of $\mathbf{W}_j(t)$ are given by $(\tilde{W}_j(t))_m = \langle ss|W_j(t)|\{p, m\}s\rangle$, and similarly $\underline{W}_j(t)$ has elements given by $\langle s\{p, m_2\}|W_1(t)|\{p, m_1\}\{p, m_2\}\rangle$.

We now take the microwave to be linearly polarized and choose our quantization axis $\hat{\mathbf{z}}$ in the direction of the polarization, i.e. $\boldsymbol{\mathcal{E}}(t) = \mathcal{E}(t)\hat{\mathbf{z}}$. Similarly as in section 2.3 we obtain for the matrix elements

$$\langle ss|\boldsymbol{\mu}_1\hat{z}|\{p, m\}s\rangle = \frac{d_{v0,v1}}{\sqrt{3}}\delta_{m0}. \quad (16)$$

From the results of section 2.3, we then note that microwave polarization along the chain (see (8)) or perpendicular to the chain (see (9)) leads to a de-coupling of the angular momentum state $m = 0$ from the other m states. Thus, we can consider the reduced Hamiltonian

$$H = \begin{bmatrix} 2E_s & \Omega_1(t) & \Omega_2(t) & 0 \\ \Omega_1(t) & (E_s + E_p) & V_{ps} & \tilde{\Omega}_2(t) \\ \Omega_2(t) & V_{ps} & (E_s + E_p) & \tilde{\Omega}_1(t) \\ 0 & \tilde{\Omega}_2(t) & \tilde{\Omega}_1(t) & 2E_p \end{bmatrix} \quad (17)$$

with $\Omega_n(t) = \frac{1}{\sqrt{3}}\mathcal{E}(t)d_{v0,v1}$ and $\tilde{\Omega}_n$ is of the order of Ω_n. It is instructive to diagonalize within the one-exciton space to obtain the 'eigenstates' $|\pm\rangle = \frac{1}{\sqrt{2}}(|\pi_1\rangle \pm |\pi_2\rangle)$ with energies

$E_\pm = (E_s + E_p) \pm V_{ps}$. Taking E_s as zero of energy we obtain for the Hamiltonian in this basis

$$H = \begin{bmatrix} 0 & \Omega_+(t) & \Omega_-(t) & 0 \\ \Omega_+(t) & E_p + V_{ps} & 0 & \tilde{\Omega}_+(t) \\ \Omega_-(t) & 0 & E_p - V_{ps} & \tilde{\Omega}_-(t) \\ 0 & \tilde{\Omega}_+(t) & \tilde{\Omega}_-(t) & 2E_p \end{bmatrix} \quad (18)$$

with $\Omega_\pm = \frac{1}{\sqrt{2}}(\Omega_1 \pm \Omega_2)$. Since we are dealing with identical atoms $\Omega_- = 0$, the microwave couples only to the symmetric state $|+\rangle = \frac{1}{\sqrt{2}}(|\pi_1\rangle + |\pi_2\rangle)$. Thus, in order to be resonant with the transition $|ss\rangle \rightarrow |+\rangle$ we will detune the microwave by V_{ps} w.r.t. the atomic transition frequency. This also means that the microwave is detuned by $2V_{ps}$ w.r.t the transition from the state $|+\rangle$ to the doubly excited state $|pp\rangle$, so that the population of the doubly excited state will be strongly suppressed.

Ideally, the microwave pulse should transfer all the population from the $|ss\rangle$ state to the $|+\rangle$ state and be so short that the atoms do not move appreciably during the duration of the pulse. We have done full numerical simulations of this excitation scheme for three lithium atoms, and we found that pulses of few nanoseconds duration can be used to achieve this goal.

It also is of interest to access the aggregate eigenstate $|-\rangle$. We will actually focus on dynamics arising from a $|-\rangle$-type initial state and interactions with $\eta = 1$ throughout this paper, since in that case the smaller energetic separation between the totally repulsive adiabatic state and its energetic neighbour leads to more interesting non-adiabatic effects. This scenario was also considered in our previous work [15, 36].

Since $|-\rangle$ does not directly couple to the linear polarized microwave, as argued above, this requires a second state preparation step in which e.g. the phase of the $|\pi_2\rangle$ component of the quantum state is inverted. This can be achieved using a Rabi-2π laser pulse, which is resonant on the transition from $|\nu p\rangle$ to e.g. the absolute ground state $|2s\rangle$ and spatially focussed to only interact with atom 2 [52].

2.7. Dynamical methods

Up to this point we have introduced the Rydberg aggregate as an ensemble of alkali atoms with parameters chosen to enable a description of collective excitations in terms of Frenkel excitons, and explained how the atoms can be brought into the required internal electronic states. To form a *flexible* Rydberg aggregate, we further wish to include motion of the atoms. We now list different possibilities of describing this motion numerically.

2.7.1. Exact solution: Schrödinger's equation.
The full quantum-mechanical many-body problem posed by the Hamiltonian (2) is conceptually straightforward, but becomes quickly intractable as the number of atoms N is increased. However, for small N, it is not difficult to directly solve the Schrödinger equation

$$i\frac{\partial}{\partial t}|\Psi\rangle = H|\Psi\rangle. \quad (19)$$

Expanding the full wavefunction in electronic (diabatic) states according to $|\Psi(\mathbf{R})\rangle = \sum_{n=1}^N \phi_n(\mathbf{R})|\pi_n\rangle$, we arrive at

$$i\frac{\partial}{\partial t}\phi_n(\mathbf{R}) = \sum_{m=1}^N \left[-\frac{\nabla_{\mathbf{R_m}}^2}{2M}\phi_n(\mathbf{R}) + V_{nm}(R_{nm})\phi_m(\mathbf{R}) \right]. \quad (20)$$

We solve (20) for three Li atoms in order to validate the quantum–classical methods presented further below, which in turn will then be faithfully used for longer chains. In practice, the irrelevant centre-of-mass degree of freedom is removed from (20) resulting in an effectively two-dimensional (2D) problem. This is solved on a discrete spatial grid.

The above *diabatic* representation of the wavefunction $\phi_n(\mathbf{R})$ allows a straightforward propagation. To interpret the results and compare them with the quantum–classical methods, it can also be beneficial to move to the *adiabatic* representation

$$|\Psi(\mathbf{R})\rangle = \sum_{k=1}^N \tilde{\phi}_k(\mathbf{R})|\varphi_k(\mathbf{R})\rangle. \quad (21)$$

The two representations are related by

$$\tilde{\phi}_k(\mathbf{R}) = \sum_n O_{kn}(\mathbf{R})\phi_n(\mathbf{R}), \quad (22)$$

with $O_{kn}(\mathbf{R}) = \langle \varphi_k(\mathbf{R}) | \pi_n \rangle$. For instance, the initial state (12) corresponds to $\tilde{\phi}_{rep}(\mathbf{R}) = \prod_{n=1}^N \phi_G(R_n)$ and $\tilde{\phi}_k(\mathbf{R}) = 0$ for $k \neq$ rep in this representation.

When analysing our results, we will not show the full N-dimensional nuclear/atomic wavefunction but focus on the more intuitive total atomic density, which is given by

$$n(R) = \sum_{j=1}^N \sum_{m=1}^N \int d^{N-1}\mathbf{R}_{\{j\}} |\phi_m(\mathbf{R})|^2. \quad (23)$$

Here, $\int d^{N-1}\mathbf{R}_{\{j\}}$ denotes integration over all but the jth nuclear coordinate. The density $n(R)$ gives the probability of finding an atom at position R.

We will assume that wavefunctions of different atoms never occupy the same space. For the calculations shown, this assumption turned out to be valid.

2.7.2. Quantum–classical propagation.
When the number of atoms N exceeds values where the direct quantum solution of the time-dependent Schrödinger equation (20) is tractable, we resort to mixed quantum–classical methods, namely the Ehrenfest method (EF) [53, 54] and Tully's fewest switching algorithm [54, 55]. In both approaches, the nuclear coordinates $\mathbf{R}$ are treated classically and an ensemble of trajectories $\mathbf{R}(t)$ is propagated in a way specified below. In order to represent the initial nuclear wave packet, we randomize the initial positions and velocities for the trajectories according to the Wigner distribution of the initial state (12). Since the spatial density of each atom is assumed to be Gaussian, this simply amounts to un-correlated Gaussian spread of both position (with standard deviation $\sigma_0/\sqrt{2}$) and velocities (with standard deviation $1/(\sqrt{2}\sigma_0 M)$). To obtain the total atomic density $n(R)$, the positions of the atoms are binned throughout all trajectories.

The excitonic propagation is done by expanding $|\Psi(\mathbf{R}, t)\rangle = \sum_{k=1}^{N} \tilde{c}_k(t)|\varphi_k(\mathbf{R})\rangle$, where the complex amplitudes $\tilde{c}_k$ are determined by

$$i\frac{\partial}{\partial t}\tilde{c}_k = U_k(\mathbf{R})\tilde{c}_k - i\sum_{q=1}^{N}\dot{\mathbf{R}} \cdot \mathbf{d}_{kq}\tilde{c}_q, \tag{24}$$

where $U_k(\mathbf{R})$ are the adiabatic potential energy surfaces defined in (10) and

$$\mathbf{d}_{kq} = \langle\varphi_k(\mathbf{R})|\nabla_{\mathbf{R}}|\varphi_q(\mathbf{R})\rangle \tag{25}$$

are the so-called non-adiabatic coupling vectors.

The two methods differ in the classical propagation method for the nuclear coordinates. In the Ehrenfest method, the nuclear dynamics is determined by Newton's equations

$$M\ddot{\mathbf{R}} = -\nabla_{\mathbf{R}}\bar{U}(\mathbf{R}, t) \tag{26}$$

with the *average* potential

$$\bar{U}(\mathbf{R}, t) = \langle\Psi(\mathbf{R}, t)|H^{\text{el}}(\mathbf{R})|\Psi(\mathbf{R}, t)\rangle = \sum_k |\tilde{c}_k(t)|^2 U_k(\mathbf{R}).$$

In contrast, in Tully's method each trajectory moves classically on a *single* adiabatic surface $U_k(\mathbf{R})$, except for the possibility of instantaneous jumps among the adiabatic states. Between jumps the classical equation of motion is

$$M\ddot{\mathbf{R}} = -\nabla_{\mathbf{R}}U_k(\mathbf{R}). \tag{27}$$

Details on Tully's method and our numerical implementation are given in appendix B. Now, when performing the average over trajectories the spreading due to the surface hopping is combined with the spreading due to different trajectories for different initial classical nuclear positions.

3. Entanglement transport

In the previous section, we have explained the design of a flexible Rydberg aggregate and our various methods for dynamical propagation. Hence, we are ready to consider the dynamical problem introduced in [36] in more detail. We study the effect of resonant dipole–dipole interactions on a regular linear chain of Rydberg atoms. Initially, we impose a 'deformation' in the distances between the atoms that gives rise to an associated localized exciton state, which is strongly repulsive. We demonstrate a strong correlation between the resulting exciton dynamics and the motion of the atoms. A combined pulse of atomic displacements ('deformation') and localized electronic excitation propagates adiabatically through the chain in a manner reminiscent of Newton's cradle. We show that this can also be viewed as adiabatic entanglement transport, since the initial electronic state $|\varphi_{\text{rep}}(\mathbf{R}, t = 0)\rangle$ is a Bell state [56]. To see this, we rewrite the initial state as

$$|\varphi_{\text{rep}}(\mathbf{R}, t = 0)\rangle \approx \frac{1}{\sqrt{2}}(|\pi_1\rangle - |\pi_2\rangle) \tag{28}$$

$$= \frac{1}{\sqrt{2}}[|\text{ps}\rangle - |\text{sp}\rangle] \otimes |\text{s}\cdots\text{s}\rangle, \tag{29}$$
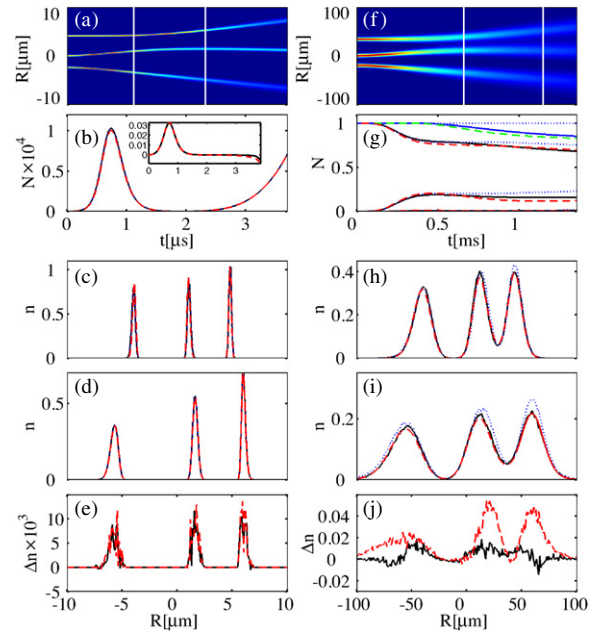

Figure 4. Comparison of QM, Tully and EF for nuclear dynamics in the case $N = 3$ for two different parameter sets, yielding adiabatic (a)–(e) and non-adiabatic dynamics (f)–(j). The time evolution of the total atomic density $n(\mathbf{R}, t)$ (a), (f) is shown together with a comparison of Tully's surface hopping calculations (black solid line) with the full quantum evolution (red dashed line) and EF (blue dotted line) in other panels. (b) Relative population on the energetically nearest adiabatic surface, $n_{\text{mid}} = \int d\mathbf{R}|\bar{\phi}_{\text{mid}}(\mathbf{R})|^2$ ($n_{\text{mid}} = |\tilde{c}_{\text{mid}}|^2$ in the Tully /EF algorithms), as a measure of the propensity of non-adiabatic transitions. The index 'mid' is defined in the text. The inset shows the differences Tully–QM (black solid line) and EF–QM (red dashed line). (g) Similar to (b) but showing the total population (Tully (blue solid line), QM (green dashed line), EF (blue dotted line)) and population of all three surfaces 'rep', 'mid', 'att' in descending order. (c), (h) Spatial slice $n(x, t_1)$, with t_1 as indicated by the first vertical white lines in (a), (f). (d), (i) Spatial slice $n(x, t_2)$, with t_2 as indicated by the second vertical white lines in (a), (f). (e), (j) Difference Tully–QM and EF–QM for the density profiles at t_2 with lines as in the inset of (b).

where the state in square brackets concerns the dislocated atoms, and $|\text{s}\cdots\text{s}\rangle$ the rest of the chain. Prior to demonstrating the combined transport of displacement, excitation and entanglement, we validate the quantum–classical methods required for larger chains.

3.1. Comparison and validation of methods

To confirm the applicability of quantum–classical numerical treatments to the dislocated chain of section 2.2, we consider the smallest nontrivial chain, namely $N = 3$. In this case, it is not difficult to solve the full Schrödinger equation numerically exactly. We are then in a position to compare all three propagation schemes outlined in section 2.7, full quantum mechanics (QM), Tully's fewest switching (Tully) and the Ehrenfest method (EF). We consider two distinct scenarios: (i) predominantly adiabatic dynamics for the validation of the quantum–classical methods for the subsequent section 3.2. (ii) Strongly non-adiabatic dynamics, in order to highlight the differences in propagation algorithms.

Scenario (i) is shown in figure 4(a)–(e). We used $M = 11\,000$ au and $\mu = 1000$ au as in [36]. The quantum-mechanical probability of finding an atom at a certain position predicted by QM and the corresponding semiclassical methods show perfect agreement. As the dynamics is almost completely adiabatic, each avoided collision between two atoms is accompanied by excitation transfer. We will highlight this in detail in the next section, where we consider longer chains. Note that Tully and EF even perfectly reproduce the small fraction of population that has switched to the neighbouring surface [4], as can be seen in figure 4(b).

For scenario (ii), shown in figure 4(f)–(j), we changed our parameters to $M = 1800$ (hydrogen) and $\mu = 200$ au. This fictitious scenario was solely chosen to increase the system's non-adiabaticity and is probably not realistic. Due to increased diffusion and collisions, we extended all three models by a phenomenological treatment of ionization, presented and justified in appendix C. It can be seen that in contrast to scenario (i), there are now significant transitions from the initial surface 'rep' to 'mid'. On this surface, the trimer no longer feels an overall repulsive potential [15]. Consequently, atoms that have undergone a change of adiabatic state can approach each other closely where they ionize. This is reflected in the drop of overall population for the QM and Tully models. In contrast, atoms in the EF model always propagate according to a state averaged potential, which due to 75% population on the repulsive surface is still dominantly repulsive. Consequently we do not observe significant ionization in the EF model. Despite this main difference, it can be seen that the overall state population as well as spatial density distribution of the exact QM model is still fairly well reproduced by both Tully and EF.

The physical situation shown in figure 4(a)–(e) is quite similar to that presented in the following section, except for the number of atoms. The quality of agreement between the three disparate methods found in the case $N = 3$ gives confidence that the quantum–classical methods will produce reliable results also for the longer chain considered next, for which a solution of the Schrödinger equation would no longer be feasible.

3.2. Coupled atomic and electronic dynamics

The atomic motion and excitation transfer for a chain of $N = 7$ atoms, when starting in the exciton state with highest energy (which corresponds to the fully repulsive state) is shown in figures 5 and 6. As expected, initially the two close atoms strongly repel each other. When atom 2 approaches atom 3 these atoms start to repel each other. Atom 2 slows down and atom 3 accelerates. In this way the momentum of atom 2 is transferred through the chain to atom 7, which is reached at $t \approx 5.5\,\mu s$. Then, atom 7 moves away from the remaining $N - 2$ atoms, as atom 1 did already at the beginning of the evolution. The remaining atoms form a regular chain with distance x_0 between the atoms and positions shifted by $x_0 - a$
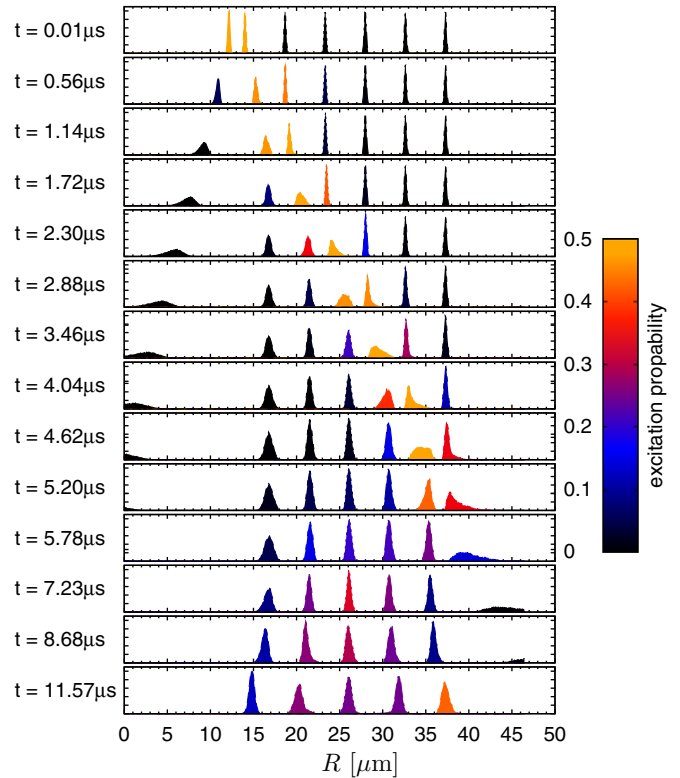

Figure 5. Dynamics of atomic motion and excitation transfer. Shown are snap-shots in time as labelled, of the total atomic density, as a function of spatial coordinate. The colour shading reflects the probability of the underlying atom to be excited, and hence demonstrates exciton transport.

w.r.t. the initial position of the respective atom. This chain is in a repulsive state and the atoms drift very slowly apart in a manner typical for a regular chain as discussed in [15].

Note the spreading of the initially quite localized wavepackets right from the start, for example atom 1. This is due to the initial *spatial* width of the Rydberg atom distribution σ_0, which gets converted into a strong velocity spread Δv due to the steep slope of the dipole–dipole potential. One expects $\Delta v = (2\sigma_0\mu^2/Ma^4)^{1/2}$. Then, estimating $\Delta x = \Delta v t$ describes the spreading of atom 1 well. Atom 2 initially obtains the same large velocity spread; in the following elastic collision this is however exchanged completely against the (narrow) velocity distribution of 3. After the dislocation has traversed the chain, only the outer atoms have a considerable spread in velocity which results in a large position smear as time progresses (see figure 5). During this transfer of momentum there is negligible overlap of the spatial distributions of different atoms, even at the avoided collisions.[5]

Up to now we have restricted our discussion to the 'slow', 'macroscopic' movement of the Rydberg atoms. The interaction strength between a pair of Rydberg atoms at a distance $a = 3.5\,\mu m$ (corresponding to the average

---

[4] For the case $N = 3$ there are three adiabatic surfaces, one overall repulsive ('rep'), one attractive ('att') and one energetically between those, which we label 'mid'.

[5] In interpreting figure 5, keep in mind that a narrow gap between the total density peaks associated with two neighbouring atoms *does not* imply that the atoms approach closely: correlations between atomic positions are strong and result in the absence of actual close encounters.
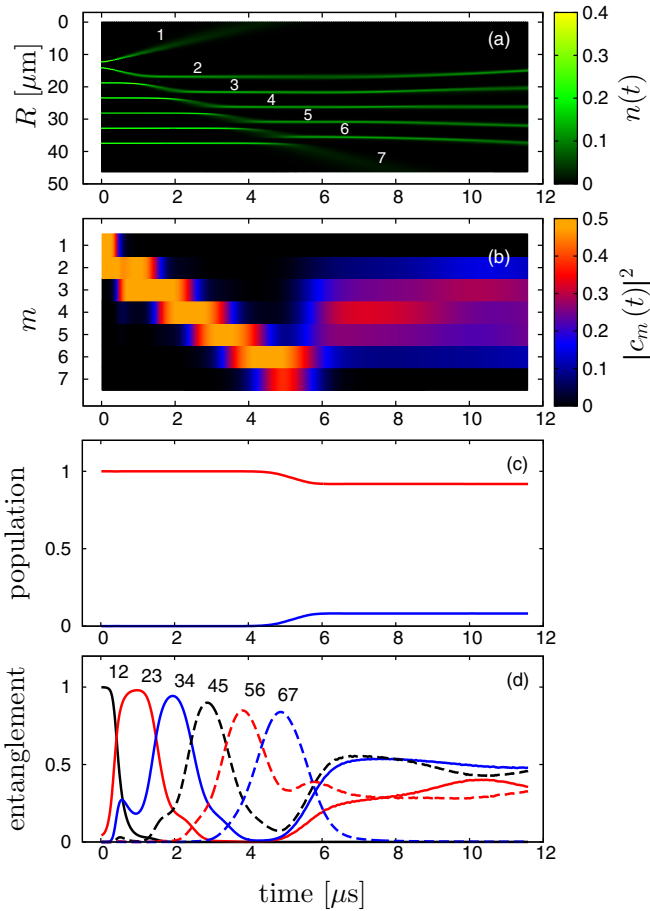
Figure 6. Dynamics of atomic motion and excitation transfer
averaged over 10^5 realizations. (a) Total atomic density as defined in
(23), obtained by binning the classical trajectories $R(t)$, see
appendix B. (b) Diabatic populations $|c_m(t)|^2$ in the localized state
basis $|\Psi(t)\rangle = \sum_n c_n(t)|\pi_n\rangle$. The row m shows the excitation
probability of the atom m. (c) Population on the adiabatic
(eigen-)surface rep (red) and the energetically next one (blue).
(d) Binary entanglement (see appendix A) $E_{n,n+1}$ for neighbouring
atoms. The pair of indices $n, n+1$ is assigned to each line near its
maximum.

closest distance between atoms up to the time $t = 5.5\,\mu s$)
is approximately 141 MHz, which corresponds to a 'transfer'
time of $0.02\,\mu s$. This is much faster than the time scale of
motion of the atoms. The colour shading in figures 5 and
6(b) visualize how the electronic excitation evolves in time.
One sees that the excitation gets transferred such that it is
always localized on the two instantaneously nearest atoms, in
accordance with the structure of exciton eigenstates outlined
in [15]. After $5.5\,\mu s$ the momentum that was transferred
through the chain kicks out the last atom, and a well-defined
close proximity pair no longer exists. The exciton state
then assumes the shape for an equidistant chain, de-localized
over the entire chain (consisting of the remaining $N - 2$
atoms), which subsequently slowly spreads out. However,
this state change is not completely adiabatic as can be seen
in figure 6(c) where the adiabatic population on the initial
(repulsive) adiabatic surface together with the population on
the neighbouring adiabatic surface is shown. One clearly sees
a change of population around $t = 5.5\,\mu s$, which is the time

when atom 7 starts to separate from the chain. The duration
over which population transfer between the surfaces occurs
corresponds to the time during which the excitation localized
on atoms 6 and 7 spreads over the remaining chain (see
figures 5 and 6(b)). This change of the adiabatic populations
can be understood in a simple way: as noted above, up to
$t \approx 5\,\mu s$ the excitonic transfer time was much faster than the
nuclear dynamics. During the time in which atom 7 leaves the
chain, however, the excitation has to delocalize over the whole
remaining chain to stay in the fully repulsive adiabatic state.
The distances involved in this redistribution of excitation are
much larger than a or x_0; hence, the electronic time scale is
slower, *now of* the order of the nuclear motion of atom 7. After
the delocalized state is reached, the relevant nuclear dynamics
becomes very slow—the system behaves adiabatic again. We
found that the magnitude of these non-adiabatic transitions
increases with chain length N if all other parameters are kept
constant, reflecting a decrease in the energetic separation of
the involved adiabatic states for larger N.

So far we have viewed the dynamics of excitation transport
essentially as a wave-spreading phenomenon on a chain whose
constituents are free to move. It is possible to give the
observed phenomenon a quite different twist, by considering
the dynamical transport of entanglement that is linked to the
excitation migration. In particular, we focus on entanglement
within the subsystem comprised of the electronic state of atoms
n and m only, denoted by $E_{n,m}$. This subsystem can contain
much less information than the full many-body quantum state;
hence, entanglement therein is expected to be more robust and
simultaneously more accessible. We summarize in appendix
A how we calculate the relevant bipartite *entanglement of
formation* [57]. As can be seen in figure 6(d), the initially
perfect entanglement between 1 and 2 is transported through
the chain with only minor losses up to the point where
the final atom leaves the chain[6]. Then the exciton state
de-localizes over the entire chain, with a resulting drop of
bipartite entanglement. A comparison of panels (b) and (d) of
figure 6 makes it apparent that entanglement is here a direct
consequence of coherent, delocalized excitation: whenever
the diabatic population on *both* members of a neighbouring
atom pair is large, so is the mutual entanglement.

4. Parameter dependence of the entanglement transport

In the following we will investigate how the coupled excitonic
and nuclear dynamics depends on the mass M of the atom,
the magnitude μ of the used transition dipole and on the
absolute initial positions of the atoms. These dependences can
in principle be studied in experiment. In addition, we will also
investigate changes of the functional form of the long-range
interaction, which is more of general theoretical interest. As
in the previous section, for the following calculations we will
use and compare the two mixed quantum–classical methods.

---

[6] We have verified that both methods outlined previously give the same
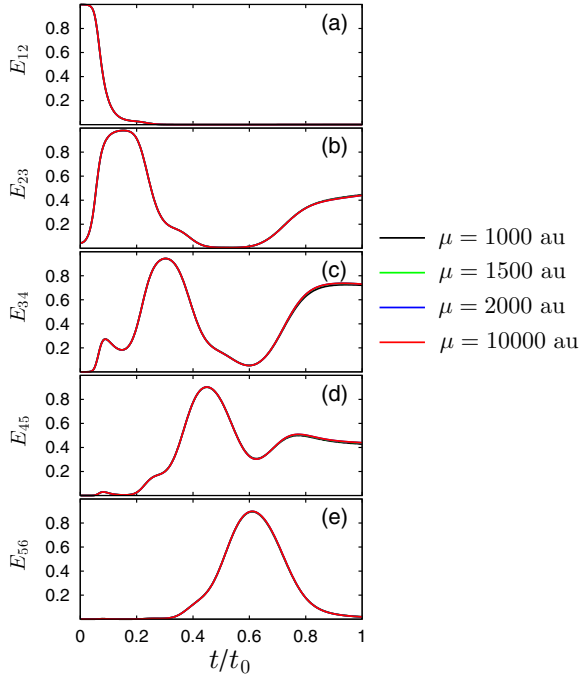entanglement evolution for the case $N = 3$.

Figure 7. Entanglement $E_{nm}(t)$ between neighbouring atoms n and m for different values of the transition dipole moment μ calculated with Tully and Ehrenfest. For each μ the time is scaled with $t_0 = t_0(\mu) = T/\mu$ with $T = 6.44\,\mu$s. The curves for different μ are indistinguishable.

Since we focus on dynamics which is more or less adiabatic, the motion of the atoms is approximately governed by

$$M\frac{\partial^2}{\partial t^2}R = -\nabla_R U_{\rm rep}(R) = -\nabla_R \frac{\mu^2}{R^3} = 3\frac{\mu^2}{R^4}, \qquad (30)$$

which is equivalent to $\frac{\partial^2}{\partial t^2}R = 3\frac{\mu^2}{MR^4}$. If we now scale

$$R_\lambda = \lambda R, \qquad (31)$$

$$M_\beta = \beta M, \qquad (32)$$

$$\mu_\gamma = \gamma \mu, \qquad (33)$$

we see that (30) remains invariant, if time is also scaled by

$$\tau = t\gamma^{-1}\beta^{1/2}\lambda^{3/2}. \qquad (34)$$

This means, for example, that for the doubled transition dipole moment μ one expects the dynamics to be twice as fast, but otherwise unchanged. This is confirmed in figure 7 where entanglement transport for various transition dipole strengths is shown, each scaled by (34).

Consider next the distance dependence. Numerical calculations are shown in figure 8. Here, we have kept the ratio a/x_0 constant and scaled the distances between the atoms according to (31); however, we did not scale the width σ_0 of the initial nuclear wavefunction. One sees that the overall dynamics obeys the scaling (34); however, there are slight differences in the magnitude of the entanglement. These are due to the different relative width of the initial Gaussian. If we also scale σ_0, we obtain perfect agreement as in figure 7.

The dependence on the mass is demonstrated in figure 9. Again one sees that the scaling relation (34) is basically
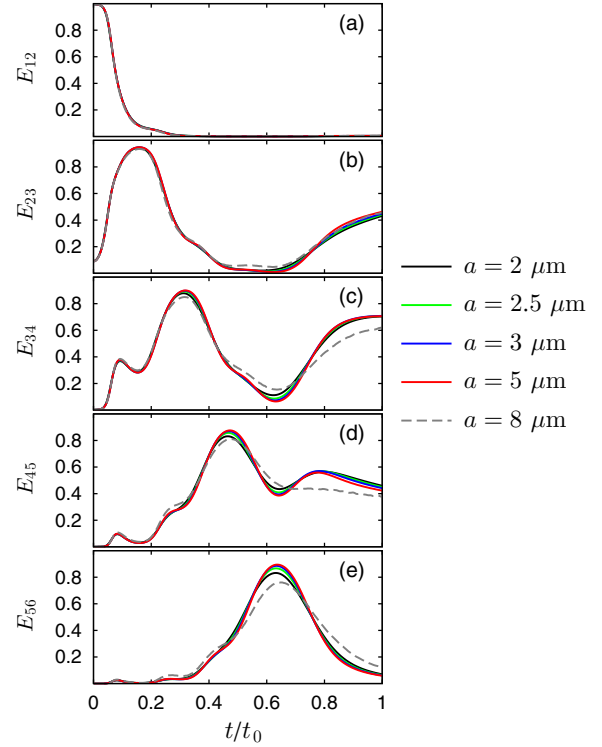

Figure 8. As figure 7 but now for scaled distances $\lambda \times 2\,\mu$m and constant a/x_0. Here, the width σ_0 of the initial nuclear wavefunction is kept constant. The time is given in units of $t_0 = t_0(\lambda) = T\lambda^{5/2}$ with T = 6.44 μs.

fulfilled; however, there are quite large changes in the absolute value of entanglement when masses or calculation methods are varied, especially after the delocalization of the excitation (see section 3.2). These differences appear pronounced for very small masses[7].

To understand the deviations, the number of jumps invoked in Tully's method is shown as a function of mass in figure 10. As expected for smaller masses the dynamics becomes more non-adiabatic and the number of jumps strongly increases[8].

From the above analysis one sees that due to an increasing number of jumps there are differences in the dynamics for different masses. However, in practice these differences are quite small as is demonstrated in figure 9. The overall shape of the curves stays the same; only the timescale for the total dynamics changes. Nevertheless one clearly sees that with smaller mass, where the dynamics becomes more non-adiabatic, there is also a larger loss of entanglement.

It is instructive also to compare Tully's surface hopping approach with the much simpler (and faster) Ehrenfest method. For larger masses, in figure 9, the results obtained from Tully's surface hopping method and the Ehrenfest-average-potential method do not differ, since only a few transitions between the adiabatic states occur. For lighter masses, where more transitions occur, the methods start to deviate, since the

---

[7] The green curve corresponds roughly to hydrogen.
[8] A similar plot but with the number of jumps reduced by roughly a factor of ten is obtained when starting from the symmetric initial electronic state, due to a larger energy separation between neighbouring surfaces.
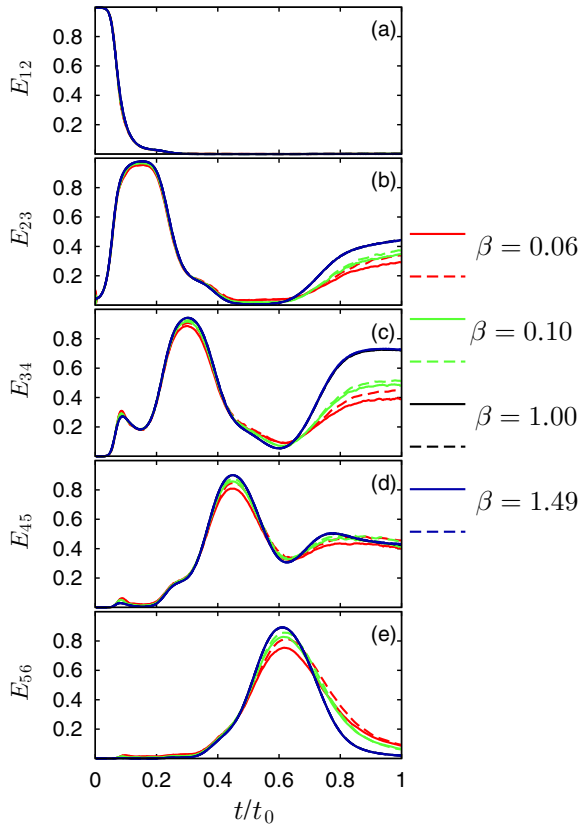
Figure 9. As figure 7 but now for different masses $M = \beta M_{Li}$. Tully's surface hopping algorithm (solid lines), Ehrenfest method (dashed lines). The time is given in units of the mass-dependent time $t_0 = t_0(\beta) = T \sqrt{\beta}$ with $T = 6.44\,\mu s$. For $m = 1$ and $m = 1.49$ all lines are indistiguishable.
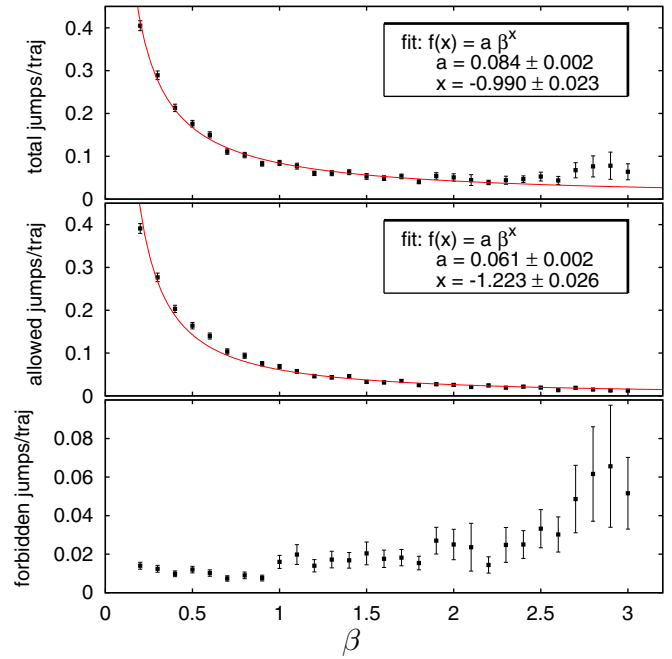

Figure 10. Number of jumps invoked in Tully's algorithm as a function of the mass. Here, $\beta = M/M_{Li}$ is the mass expressed in units of the mass of lithium. The black squares are the numerical data (with statistical errors) and the red lines are power law fits.

dynamics on the averaged potential in the Ehrenfest method differs from that stemming from Tully's algorithm.

4.1. Dependence on the interaction potential

The physical transition dipole–dipole interaction between the states $|\pi_n\rangle$ scales with $1/R^3$, where R is the distance between two Rydberg atoms. In the following we will investigate (hypothetical) resonant energy transfer interactions with power law dependence on the distance

$$V_{nm} = -\mu^2 / R_{nm}^\alpha. \tag{35}$$

As already shown in figure 2, to obtain the initial state $|\psi_{ini}\rangle \approx (|\pi_1\rangle - |\pi_2\rangle)/\sqrt{2}$, the ratio a/x_0 has to be decreased for decreasing α. We choose a/x_0 such that the ratio of the interaction energy between atoms 1 and 2 to that between atoms 2 and 3 is kept constant as α varies. Parameters selected in this manner are shown in figure 2 as solid black bars.

To have comparable dynamics for different exponents α, we further fix the values of a and x_0. We choose the α-dependent initial distance a_α by requiring $V_{12}(a_\alpha) \equiv V_{12}(a_3)$, which leads to $a_\alpha = (a_3)^{3/\alpha}$. Furthermore, we have to adapt the width of the initial nuclear wave packet to the new distance. Our variance σ_α of the Gaussian position distribution is determined by requiring that the corresponding spread of

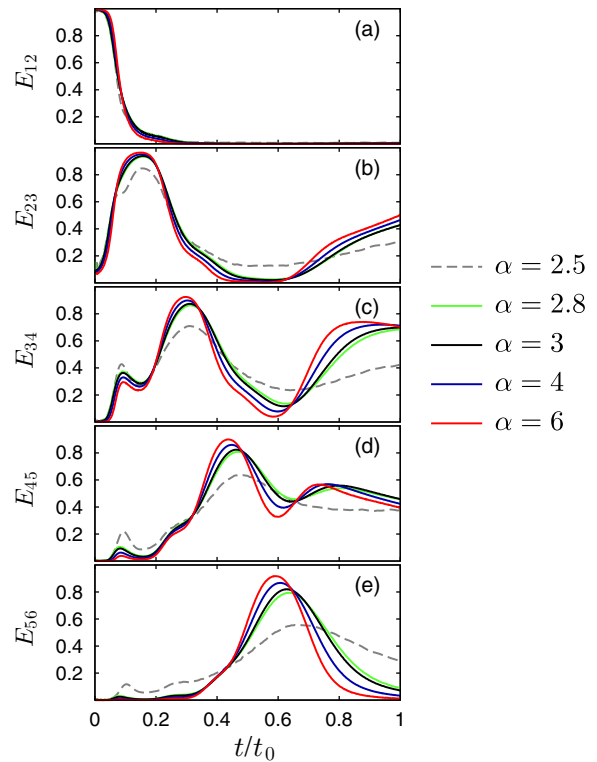

Figure 11. As figure 7 but now for different exponents α. The time is scaled according to (36).

initial potential energies is roughly independent of α. This leads to the condition $\sigma_\alpha \approx \frac{3}{\alpha} a_3^{\frac{3}{\alpha}-1} \sigma_3$.

In figure 11, the entanglement between neighbouring atoms is shown for different α and $M = M_{Li}$. The time is

in units of $t_0(\alpha)$, which is different for each α

$$t_0(\alpha) = \frac{\alpha}{3} \sqrt{(a_3 d_3)^{1-\frac{3}{\alpha}}} \; T \qquad (36)$$

with $T = 6.44 \, \mu$s. One sees that in these scaled time units, for $\alpha \geqslant 3$, the transport of entanglement is more or less independent of α. For smaller α, however, the entanglement transport is strongly reduced.

5. Conclusions and outlook

We have demonstrated a strong connection between the motion of a chain (aggregate) of Rydberg atoms and the coherent propagation of a single electronic excitation within the chain. Adiabatic transport ensures that the excitation remains spatially localized near a dislocation passing through the chain. Our results were obtained with Tully's surface hopping method [54, 55] and the Ehrenfest method [53, 54], both of which we vindicate by comparison with exact quantum calculations for a smaller model system with similar dynamics. A key feature of our setup is that the initial state is a repulsive electronic eigenstate of the chain.

If the system was not prepared in an electronic eigenstate but in a state where the excitation is localized on a single atom, one would find a fast excitation transfer similar to that described e.g. in [24, 58]. If free motion is added to such a scenario, however, those parts of the population that necessarily initially reside on an attractive surface can lead to fast collisions of light atoms. In that case the dynamics could be treated with the Tully algorithm; however, the Ehrenfest method would fail (e.g. for the dimer there would be no movement at all).

We wish to contrast the results of this study with those obtained in [10] for van der Waals interactions. For the case of the repulsive van der Waals interaction one finds similar trajectories for the movement of the atoms, showing for example Newton's cradle-like transfer of a dislocation through an atomic chain. The crucial difference to the dipole–dipole coupling presented here is the excitation energy transfer involved in the latter. Even more important is that the dynamics in the dipole–dipole case depends on the electronic state. An even stronger contrast to van der Waals is found for initial states other than the fully repulsive one treated here. Even mixed, partially attractive, partially repulsive dynamics is possible as shown by Ates *et al* [15]. Such dynamics would arise from scenarios presented here only if a sufficient fraction of the atoms has undergone non-adiabatic transitions to other potential surfaces (as in our figure 4(d)).

In this paper, we have exclusively studied free Rydberg atoms. When the atoms are trapped, the dipole–dipole forces will induce oscillations of atoms in the traps, which in turn lead to oscillating couplings and again to a correlation between the motion of the exciton and the motion of the Rydberg atoms. This gives rise to the well-known Davydov soliton [59, 60]. Constructing large 'crystals' of N Rydberg atoms is problematic since each atom has a finite lifetime τ, leading to an even shorter lifetime of the crystal of τ/N. Therefore, it would be advantageous to map the strong dipole–dipole

interaction in the Rydberg state to the ground state using off-resonant laser dressing techniques [61]. Using this technique and a ring geometry, it is even possible to use (dressed) Rydberg aggregates for the study of near conical-intersection dynamics [62]. For the parameters used in our simulations of section 3, we expect the lifetime to be sufficient.

Experimentally, observables as shown in figure 6 could be monitored using techniques for the simultaneous position and state measurement of Rydberg atoms [63]. In our particular system the presence of entanglement can then be directly inferred from the state populations.

Appendix A. Entanglement of formation

The 'entanglement of formation' [57, 64] is an entanglement measure for bipartite quantum states, also applicable to mixed states. For a pure state it equals 1 for perfect entanglement and it is 0 for a separable state.

We calculate this entanglement measure in the following way: first consider the reduced density matrix describing the electronic state when the atomic positions are traced out:

$$\hat{\sigma} = \sum_{n,m} \sigma_{nm} |\pi_n\rangle\langle\pi_m|, \qquad (A.1)$$

with

$$\sigma_{nm} = \begin{cases} \int \mathrm{d}^N \mathbf{R} \; \phi_n^*(\mathbf{R})\phi_m(\mathbf{R}) & \text{QM} \\ \overline{c_n^* c_m} & \text{Tully/Ehrenfest.} \end{cases} \qquad (A.2)$$

The first expression holds for the full quantum calculations, and the second for the quantum–classical methods. In the latter case $\overline{\cdots}$ denotes the trajectory average and $c_n = \sum_k O_{nk}^T \tilde{c}_k$ are the coefficients in the diabatic basis with O_{nk} defined in (22).

From (A.2) we construct the binary-reduced electronic density matrix of atoms a and b:

$$\hat{\beta}_{ab} = \mathrm{Tr}^{\{a,b\}}[\hat{\sigma}]. \qquad (A.3)$$

The symbol $\mathrm{Tr}^{\{a,b\}}[\cdots]$ denotes the trace over the electronic states for all atoms other than a, b. Recall that in the present approach each atom is described by a two-level system as discussed in subsections 2.2–2.6. With our labels for those two states, $|s\rangle$ and $|p\rangle$, the trace appearing in (A.3) is over the Hilbert space spanned by the basis $\{|n_1\rangle \cdots |n_N\rangle, \; n_j \in \mathrm{s, p}\}$.

The remaining reduced subspace of atoms a and b is spanned by $|pp\rangle, |ps\rangle, |sp\rangle, |ss\rangle$. Since the states $|\pi_n\rangle$ appearing in (A.1) only contain a single excitation p, all matrix elements of $\hat{\beta}_{ab}$ involving $|pp\rangle$ vanish. In the reduced basis one finally has

$$\hat{\beta}_{ab} = \begin{pmatrix} 0 & 0 & 0 & 0 \\ 0 & \sigma_{aa} & \sigma_{ab} & 0 \\ 0 & \sigma_{ab}^* & \sigma_{bb} & 0 \\ 0 & 0 & 0 & \sum_{c \neq \{a,b\}} \sigma_{cc} \end{pmatrix}. \qquad (A.4)$$

From this we construct

$$S_{ab} = \sqrt{\sqrt{\hat{\beta}_{ab}} \hat{\beta}_{ab}^* \sqrt{\hat{\beta}_{ab}}}, \qquad (A.5)$$

$$C_{ab} = \max(0, 2\lambda_{ab} - \mathrm{Tr} S_{ab}), \qquad (A.6)$$

with the further definitions

$$H(x) = -[x \log_2 x + (1-x) \log_2(1-x)], \quad \text{(A.7)}$$

$$\mathcal{E}(x) = H(1/2 + \sqrt{1-x^2}/2), \quad \text{(A.8)}$$

where λ_{ab} denotes the largest eigenvalue of S_{ab}; we can finally obtain the binary entanglement of the electronic states of atoms a and b:

$$E_{ab} = \mathcal{E}(C_{ab}). \quad \text{(A.9)}$$

For further details we refer to [57, 64].

Appendix B. Tully's surface hopping

The quantum-mechanical dynamics governed by (24) and the classical equation of motion (27) are solved self-consistently. The atoms move on a single adiabatic potential surface k, which however may be changed via sudden jumps to another surface q. The probability for a jump from state k to state q is given by

$$g_{kq} = \max\left(0, \frac{b_{qk}\Delta t}{a_{kk}}\right), \quad \text{(B.1)}$$

where Δt denotes the propagation time step and

$$b_{qk} = -2 \operatorname{Re}(a_{qk}^* \dot{\mathbf{R}} \cdot \mathbf{d}_{qk}), \quad \text{(B.2)}$$

$$a_{qk} = c_q c_k^*. \quad \text{(B.3)}$$

To determine if during a time step a jump takes place we compare g_{kq} with a uniform random number $\xi \in [0, 1]$. If $\xi \leqslant g_{k1}$, the jump is to the surface $q = 1$, if $g_{k1} < \xi \leqslant g_{k1} + g_{k2}$, to $q = 2$ and so forth. When a switch takes place the velocity $\dot{\mathbf{R}}$ is adjusted in order to conserve the total amount of energy. This will be done in the direction of the non-adiabatic coupling vector $\mathbf{d}_{kq}$ as follows:

$$\dot{\mathbf{R}}(t) = \dot{\mathbf{R}}(t - \Delta t) - \frac{\gamma_{kq} \mathbf{d}_{kq}}{M}. \quad \text{(B.4)}$$

Here

$$\gamma_{kq} = \frac{\beta_{kq} \pm \sqrt{\beta_{kq}^2 + 4\alpha_{kq}(U_k - U_q)}}{2\alpha_{kq}}, \quad \beta_{kq} \lessgtr 0, \quad \text{(B.5)}$$

with

$$\alpha_{kq} = \frac{1}{2M} \sum_{i=1}^{N} |d_{kq}^{(i)}|^2 \quad \text{(B.6)}$$

$$\beta_{kq} = \sum_{i=1}^{N} \dot{R}_i \cdot d_{kq}^{(i)}. \quad \text{(B.7)}$$

If the energy of the final surface q is larger than that of the initial surface k and the velocity reduction required is greater than the component of velocity to be adjusted, then the jump is rejected and instead of (B.5) we use

$$\gamma_{kq} = \frac{\beta_{kq}}{\alpha_{kq}}, \quad \text{(B.8)}$$

which corresponds to a reflection of the velocity component along $\mathbf{d}_{kq}$. Further details about Tully's algorithm can be found e.g. in [54, 55].

As described in [65] the forces $\nabla_{\mathbf{R}} U_k(\mathbf{R}) = \nabla_{\mathbf{R}} \langle \varphi_k(\mathbf{R})|H^{\mathrm{el}}(\mathbf{R})|\varphi_k(\mathbf{R})\rangle$ and the non-adiabatic coupling vectors $\mathbf{d}_{ij}$ are calculated using the Hellman–Feynman theorem. One then finds

$$\nabla_{\mathbf{R}} U_k(\mathbf{R}) = \langle \varphi_m(\mathbf{R})|(\nabla_{\mathbf{R}} H^{\mathrm{el}}(\mathbf{R}))|\varphi_m(\mathbf{R})\rangle \quad \text{(B.9)}$$

and

$$\mathbf{d}_{kq} = \frac{\langle \varphi_i(\mathbf{R})|(\nabla_{\mathbf{R}} H^{\mathrm{el}}(\mathbf{R}))|\varphi_j(\mathbf{R})\rangle}{U_j(\mathbf{R}) - U_i(\mathbf{R})}. \quad \text{(B.10)}$$

The total density $n(\mathbf{R}, t)$, as defined in (23), is obtained through a binning of the single trajectories, which means for each time step our spatial domain is discretized into bins and if a trajectory $\mathbf{R}(t) = (\mathbf{R_1(t)} \ldots \mathbf{R_N(t)})^T$ lies within such a bin, $n(\mathbf{R}, t)$ for that bin will be increased by 1. By normalizing $n(\mathbf{R}, t)$ one obtains the probability of finding an atom at a given time in a certain interval of space.

Appendix C. Phenomenological model of ionization

Our essential state model as justified in section 2.4 is only valid while atoms do not approach each other closely. Once they do, dipole–dipole shifts of all electronic states become too large to work in a small Hilbert space of electronic states. The most prominent consequence is collisional ionization of Rydberg atoms [10]. In order to avoid excursions of our numerical propagation schemes into realms where the underlying model is invalid, we incorporate a simple, phenomenological treatment of ionization for very close atoms.

For the quantum-mechanical calculations, we employ an imaginary absorbing potential of the form

$$i\frac{\partial}{\partial t} \phi_n(\mathbf{R}) = \ldots - iW(\mathbf{R})\phi_n(\mathbf{R}) \quad \text{(C.1)}$$

into (20). The shape of $W(\mathbf{R})$ is chosen to minimize reflection, while fully removing components of the wavefunction that correspond to atoms closer than an enforced minimal distance. For the data of figure 4(f)–(j), where the ionization is most important, this distance is $2\,\mu$m. For the two quantum–classical trajectory methods (EF, Tully), we incorporate the effect described by (C.1) through a stochastic 'ionization probability' $2W(x)\Delta t$ in each discrete time step of duration Δt.

Note that we do *not* aim to model realistic ionization rates; however, we *do* employ the same model of ionization in all three methods (QM, EF, Tully). Further we point out that this approach practically leads to ionization of all N atoms, even if only two atoms collided. A physically correct treatment would require a density matrix formalism, going far beyond our goal, to simply exclude numerical data from unrealistic regions of the model.

References

[1] Lukin M D, Fleischhauer M, Côté R, Duan L M, Jaksch D, Cirac J I and Zoller P 2001 Dipole blockade and quantum information processing in mesoscopic atomic ensembles *Phys. Rev. Lett.* **87** 037901

[2] Urban E, Johnson T A, Henage T, Isenhower L, Yavuz D D, Walker T G and Saffmann M 2009 Observation of Rydberg blockade between two atoms *Nat. Phys.* **5** 110

[3] Gaëtan A, Miroshnychenko Y, Wilk T, Chotia A, Viteau M, Comparat D, Pillet P, Browaeys A and Grangier P 2009 Observation of collective excitation of two individual atoms in the Rydberg blockade regime *Nat. Phys.* **5** 115

[4] Greene C H, Dickinson A S and Sadeghpour H R 2000 Creation of polar and nonpolar ultra-long-range Rydberg molecules *Phys. Rev. Lett.* **85** 2458

[5] Liu I C H, Stanojevic J and Rost J M 2009 Ultra-long-range Rydberg trimers with a repulsive two-body interaction *Phys. Rev. Lett.* **102** 173001

[6] Bendkowsky V *et al* 2010 Rydberg trimers and excited dimers bound by internal quantum reflection *Phys. Rev. Lett.* **105** 163201

[7] Anderson W R, Veale J R and Gallagher T F 1998 Resonant dipole–dipole energy transfer in a nearly frozen Rydberg gas *Phys. Rev. Lett.* **80** 249

[8] Li W, Tanner P J and Gallagher T F 2005 Dipole–dipole excitation and ionization in an ultracold gas of Rydberg atoms *Phys. Rev. Lett.* **94** 173001

[9] Robicheaux F, Hernandez J V, Topcu T and Noordam L D 2004 Simulation of coherent interactions between Rydberg atoms *Phys. Rev.* A **70** 042703

[10] Amthor T, Reetz-Lamour M, Giese C and Weidemüller M 2007 Modeling many-particle mechanical effects of an interacting Rydberg gas *Phys. Rev.* A **76** 054702

[11] Schempp H, Günter G, Hofmann C S, Giese C, Saliba S D, DePaola B D, Amthor T, Weidemüller M, Sevinçli S and Pohl T 2010 Coherent population trapping with controlled interparticle interactions *Phys. Rev. Lett.* **104** 173602

[12] Lesanovsky I 2011 Many-body spin interactions and the ground state of a dense Rydberg lattice gas *Phys. Rev. Lett.* **106** 025301

[13] Henkel N, Nath R and Pohl T 2010 Three-dimensional roton excitations and supersolid formation in Rydberg-excited Bose–Einstein condensates *Phys. Rev. Lett.* **104** 053004

[14] Mülken O, Blumen A, Amthor T, Giese C, Reetz-Lamour M and Weidemüller M 2007 Survival probabilities in coherent exciton transfer with trapping *Phys. Rev. Lett.* **99** 090601

[15] Ates C, Eisfeld A and Rost J M 2008 Motion of Rydberg atoms induced by resonant dipole–dipole interactions *New J. Phys.* **10** 045030

[16] Frenkel J 1930 Zur Theorie der Resonanzverbreiterung von Spektrallinien *Z. Phys.* A **59** 198

[17] Frenkel J 1931 On the transformation of light into heat in solids. I *Phys. Rev.* **37** 17

[18] Franck J and Teller E 1938 Migration and photochemical action of excitation energy in crystals *J. Chem. Phys.* **6** 861

[19] Davydov A 1962 *Theory of Molecular Excitons* (New York: McGraw-Hill)

[20] van Amerongen H, Valkunas L and van Grondelle R 2000 *Photosynthetic Excitons* (Singapore: World Scientific)

[21] Kobayashi T (ed) 1996 *J-Aggregates* (Singapore: World Scientific)

[22] Bierman A 1967 Motion of vibrationally coupled excition wave packet in an infinite 1-dimensional crystal *J. Chem. Phys.* **46** 1484

[23] Haken H and Reineker P 1971 The coupled coherent and incoherent motion of excitons and its influence on the line shape of optical absorption *Z. Phys.* A **249** 253

[24] Roden J, Eisfeld A, Wolff W and Strunz W T 2009 Influence of complex exciton–phonon coupling on optical absorption and energy transfer of quantum aggregates *Phys. Rev. Lett.* **103** 058301

[25] Rebentrost P, Chakraborty R and Aspuru-Guzik A 2009 Non-Markovian quantum jumps in excitonic energy transfer *J. Chem. Phys.* **131** 184102

[26] Blumen A and Silbey R 1978 Exciton line shapes and migration with stochastic exciton lattice coupling *J. Chem. Phys.* **69** 3589

[27] Barvík I and Szöcs V 1987 Coherent and incoherent exciton motion in the framework of the continuous-time random walk *Phys. Lett.* A **125** 339

[28] Hofelich F 1966 Die Bewegung eines Exzitons entlang eines Polymers unter dem Einflu der Gitterschwingungen *Z. Phys. B: Phys. Kondens. Mater.* **5** 208

[29] Eisfeld A and Briggs J S 2002 The J-band of organic dyes: lineshape and coherence length *Chem. Phys.* **281** 61

[30] Caruso F, Chin A W, Datta A, Huelga S F and Plenio M B 2009 Highly efficient energy excitation transfer in light-harvesting complexes: The fundamental role of noise-assisted transport *J. Chem. Phys.* **131** 105106

[31] Sarovar M, Ishizaki A, Fleming G R and Whaley K B 2010 Quantum entanglement in photosynthetic light harvesting complexes *Nat. Phys.* **6** 462

[32] Engel G S, Calhoun T R, Read E L, Ahn T-K, Mančal T, Cheng Y-C, Blankenship R E and Fleming G R 2007 Evidence for wavelike energy transfer through quantum coherence in photosynthetic systems *Nature* **446** 782

[33] Lee H, Cheng Y-C and Fleming G R 2007 Coherence dynamics in photosynthesis: protein protection of excitonic coherence *Science* **316** 1462

[34] Collini E and Scholes G D 2009 Coherent intrachain energy migration in a conjugated polymer at room temperature *Science* **323** 369

[35] Li W H, Tanner P J and Gallagher T F 2005 Dipole–dipole excitation and ionization in an ultracold gas of Rydberg atoms *Phys. Rev. Lett.* **94** 173001

[36] Wüster S, Ates C, Eisfeld A and Rost J M 2010 Newton's cradle and entanglement transport in flexible Rydberg aggregates *Phys. Rev. Lett.* **105** 053004

[37] Asadian A, Tiersch M, Guerreschi G G, Cai J, Popescu S and Briegel H J 2010 Motional effects on the efficiency of excitation transfer *New J. Phys.* **12** 075019

[38] Schwoerer M and Wolf H 2006 *Organic Molecular Solids* (New York: Wiley-VCH)

[39] Eisele D M, Knoester J, Kirstein S, Rabe J P and Vanden Bout D A 2009 Uniform exciton fluorescence from individual molecular nanotubes immobilized on solid substrates *Nat. Nanotechnol.* **4** 658

[40] Tani T 1996 J-aggregates in spectral sensitization of photographic materials *J-Aggregates* ed T Kobayashi (Singapore: World Scientific)

[41] Takechi K, Sudeep P K and Kamat P V 2006 Harvesting infrared photons with tricarbocyanine dye clusters *J. Phys. Chem.* B **110** 16169

[42] Reers M, Smith T W and Chen L B 1991 J-aggregate formation of a carbocyanine as a quantitative fluorescent indicator of membrane-potential *Biochemistry* **30** 4480

[43] Dedov V N, Cox G C and Roufogalis B D 2001 Visualisation of mitochondria in living neurons with single- and two-photon fluorescence laser microscopy *Micron* **32** 653

[44] Rylova S N, Amalfitano A, Persaud-Sawin D-A, Guo W-X, Chang J, Jansen P J, Proia A D and Boustany R-M 2002 The CLN3 gene is a novel molecular target for cancer drug discovery *Cancer Res.* **62** 801

[45] Dähne S 2002 Nanostrukturierte J-Aggregate als potenzielle Lichtsammelsysteme für Photosynthesen *Bunsen-Magazin* **4** 81

[46] Kirstein S and Dähne S 2006 J-aggregates of amphiphilic cyanine dyes: self-organization of artificial light harvesting complexes *Int. J. Photoenergy* **2006** 20363

[47] Roden J, Eisfeld A, Dvořák M, Bünermann O and Stienkemeier F 2011 Vibronic line shapes of PTCDA oligomers in helium nanodroplets *J. Chem. Phys.* **134** 054907

[48] Engel G S, Calhoun T R, Read E L, Ahn T K, Mančal T, Cheng Y C, Blankenship R E and Fleming G R 2007 Evidence for wavelike energy transfer through quantum coherence in photosynthetic systems *Nature* **446** 782

[49] Birkl G and Fortágh J 2007 Micro traps for quantum information processing and precision force sensing *Laser Photon. Rev.* **1** 12

[50] Stevens G D, Iu C, Bergeman T, Metcalf H J, Seipp I, Taylor K T and Delande D 1996 Precision measurements on lithium atoms in an electric field compared with R-matrix and other Stark theories *Phys. Rev.* A **53** 1349

[51] Amthor T, Reetz-Lamour M, Westermann S, Denskat J and Weidemúller M 2007 Mechanical effect of van der Waals interactions observed in real time in an ultracold Rydberg gas *Phys. Rev. Lett.* **98** 023004

[52] Kruse J, Gierl C, Schlosser M and Birkl G 2010 Reconfigurable site-selective manipulation of atomic quantum systems in two-dimensional arrays of dipole traps *Phys. Rev.* A **81** 060308

[53] Topaler M S, Allison T C, Schwenke D W and Truhlar D G 1998 What is the best semiclassical method for photochemical dynamics of systems with conical intersections? *J. Chem. Phys.* **109** 3321

[54] Tully J C and Preston R K 1971 Trajectory surface hopping approach to nonadiabatic molecular collisions: the reaction of H$^+$ with D$_2$ *J. Chem. Phys.* **55** 562

[55] Tully J C 1990 Molecular dynamics with electronic transitions *J. Chem. Phys.* **93** 1061

[56] Nielson M A and Chuang I L 2000 *Quantum Computation and Quantum Information* (Cambridge: Cambridge University Press)

[57] Hill S and Wootters W K 1997 Entanglement of a pair of quantum bits *Phys. Rev. Lett.* **78** 5022

[58] Eisfeld A 2011 Phase directed excitonic transport and its limitations due to environmental influence *Chem. Phys.* **379** 33

[59] Davydov A S and Kislukha N I 1973 Solitary excitons in one-dimensional molecular chains *Phys. Status Solidi* b **59** 465

[60] Weidlich W and Heudorfer W 1974 Coherent exciton–phonon pulse propagation in one dimension *Z. Phys.* **268** 133

[61] Wüster S, Ates C, Eisfeld A and Rost J M 2010 Excitation transport through Rydberg dressing arXiv:1011.5483

[62] Wüster S, Eisfeld A and Rost J M 2011 Conical intersections in an ultracold gas *Phys. Rev. Lett.* **106** 153002

[63] van Ditzhuijzen C, Koenderink A, Noordam L and van Linden van den Heuvell H 2006 Simultaneous position and state measurement of Rydberg atoms *Eur. Phys. J.* D **40** 13

[64] Wootters W K 1998 Entanglement of formation of an arbitrary state of two qubits *Phys. Rev. Lett.* **80** 2245

[65] Hammes-Schiffer S and Tully J C 1994 Proton-transfer in solution: molecular dynamics with quantum transitions *J. Chem. Phys.* **101** 4657